

See discussions, stats, and author profiles for this publication at: <https://www.researchgate.net/publication/231710055>

# Morphological Structure Induced by Combined Crystallization and Liquid–Liquid Demixing in Poly(ethylene terephthalate)/Poly(ether imide) Blends

ARTICLE *in* MACROMOLECULES · AUGUST 1998

Impact Factor: 5.8 · DOI: 10.1021/ma980700c

---

CITATIONS

39

---

READS

19

2 AUTHORS, INCLUDING:



Ming-Siao Hsiao

Air Force Research Laboratory, WPAFB

22 PUBLICATIONS 307 CITATIONS

SEE PROFILE

# Morphological Structure Induced by Combined Crystallization and Liquid–Liquid Demixing in Poly(ethylene terephthalate)/Poly(ether imide) Blends

Hsin-Lung Chen\* and Ming-Siao Hsiao

Department of Chemical Engineering, National Tsing Hua University,  
Hsin-Chu 30043, Taiwan, R.O.C.

Received May 4, 1998; Revised Manuscript Received June 26, 1998

**ABSTRACT:** The binary blends of poly(ethylene terephthalate) (PET) and poly(ether imide) (PEI) were miscible in the melt but showed simultaneous crystallization and liquid–liquid demixing below the melting point. In this study, the morphological structure induced by the coupling of crystallization and liquid–liquid phase separation in PET/PEI blends was probed by small-angle X-ray scattering (SAXS). For the semicrystalline blends, a drastic intensity rise at low scattering angle superposed the scattering peak associated with the lamellar stacks. This low-angular scattering was attributed to the electron density contrast between the “lamellar stack domains” (LS domains) consisting of alternating crystalline/amorphous layers and the PEI-rich domains located outside the LS domains. The scattering profiles were deconvoluted by applying the Debye–Bueche model to calculate the scattering intensity associated with the contrast between LS domains and PEI-rich domains. The morphological parameters, such as crystal thickness, amorphous layer thickness, and long period, were subsequently determined from the intensity profile obtained by subtracting the Debye–Bueche contribution from the overall scattering pattern. The crystal thickness of PET was unperturbed upon blending with PEI. A larger amorphous layer thickness was identified in the blends, showing that some PEI was incorporated inside the interlamellar regions after crystallization. Despite the swelling of the amorphous layer, the amorphous layer thickness was relatively independent of the overall blend composition. Determination of the volume fraction of lamellar stacks from SAXS linear crystallinity and bulk crystallinity revealed the occurrence of significant extralamellar placement of PEI when the overall PEI composition exceeded 20 wt %. This morphological structure is interpreted in terms of the simultaneous occurrence of liquid–liquid demixing and crystallization.

## Introduction

Based on the crystallizability of the constituents, binary polymer blends can be categorized into amorphous/amorphous, crystalline/amorphous, and crystalline/crystalline systems. For amorphous/amorphous blends, the morphology can be generated by means of a liquid–liquid demixing process such as spinodal decomposition or nucleation and growth. For the blends containing crystallizable constituents, the occurrence of liquid–solid phase separation offers another route to produce a wide variety of morphological patterns.<sup>1–8</sup> In crystalline/amorphous systems, for example, different distances associated with the exclusions of amorphous diluent may lead to interlamellar, interfibrillar, and interspherulitic incorporation of the diluent.<sup>2,7–8</sup> These morphological patterns represent various degrees of dispersion for the diluent and may lead to different properties. In the case of crystalline/crystalline systems, where cocrystallization is not present, the simultaneous crystallization of the two components creates two crystal species (A and B). The morphological pattern may be characterized by the arrangement of the two crystal species, where the configuration can be random (..ABAABABB..), alternating (ABABAB), or block (AAAAABBBBB), depending on the mutual exclusion distance of the two components during crystallization.<sup>5,6</sup> Again, different types of arrangement correspond to different degrees of dispersion for the crystal species and may give rise to different properties.

In addition to liquid–solid phase separation, morphological formation in crystalline polymer blends may sometimes be intervened by a liquid–liquid demixing process.<sup>9–18</sup> Crystallization may proceed simultaneously and compete with liquid–liquid demixing because the blend exhibits limited liquid–liquid miscibility below the equilibrium melting point.<sup>13</sup> The competitive effect of the two processes may create unique morphological patterns that are not attainable by either process alone. Hashimoto et al. demonstrated the morphological control by combined crystallization and spinodal decomposition in isotactic polypropylene (i-PP)/ethylene–propylene copolymer blends.<sup>10,11</sup> This binary pair showed interconnected domains after solvent cast. The interconnected domains gradually coarsened in the melt but they can be locked in by allowing i-PP to crystallize at temperatures below the melting point. The blend of polycaprolactone (PCL) and polystyrene oligomer (PSO) represents another system that displayed combined crystallization and liquid–liquid demixing.<sup>9,12,14–17</sup> This binary blend exhibited an upper critical solution temperature (UCST) phase diagram with the binodal lines intersecting the melting point depression curve. Observations of the spherulite morphology by Tanaka and Nishi<sup>9,12</sup> indicated that the PSO-rich phase, characterized by the liquid droplets, may be located at the spherulite front or inside the spherulites, depending on the crystallization temperatures. Nojima et al.<sup>15–17</sup> have utilized small-angle X-ray scattering (SAXS) to probe the microstructure of semicrystalline PCL/PSO systems. When the composition of PSO exceeded 15%,

\* To whom correspondence should be addressed.

a strong scattering at low scattering angle was found to superpose the scattering peak associated with the alternating crystalline/amorphous layers. The low-angular scattering was interpreted on the basis of the biphasic structure induced by combined crystallization and liquid–liquid demixing.<sup>16</sup>

In a recent study, we observed that the binary blends of poly(ethylene terephthalate) (PET) and poly(ether imide) (PEI) also exhibited combined crystallization and liquid–liquid demixing, where a UCST phase diagram was located below the melting point.<sup>18</sup> In contrast to PCL/PSO systems where the PSO-rich phase was characterized by discontinuous droplets, the PEI-rich phase was manifested by the highly interconnected domains induced by spinodal decomposition. The crystallization of PET was fast enough to lock in the interconnected domains so that the modulated morphology was preserved. Although the morphological pattern in the order of micrometers had been revealed for this system, the microstructure of a finer scale still requires further exploration. In the present study, we report the SAXS investigations of semicrystalline PET/PEI blends. The morphological parameters, such as the crystal thickness and the amorphous layer thickness, are determined from the approach of interphase distribution function.<sup>8,19–21</sup> The characteristics of the SAXS profiles as well as the composition dependences of the morphological parameters will be discussed based on the effect of combined crystallization and liquid–liquid demixing.

## Experimental Section

**Materials and Sample Preparation.** PET with the molecular weight of  $\sim 20\,000$  was obtained from Nan Ya Plastics Company Ltd., Taiwan. PEI was acquired from General Electric (GE, Ultem 1000), and its number- and weight-average molecular weights were  $M_n = 12\,000$  and  $M_w = 30\,000$ , respectively.

The PET/PEI blends were prepared by solution precipitation. PET and PEI were dissolved in phenol/tetrachloroethane (60/40 v/v) mixed solvent at  $80\text{ }^\circ\text{C}$ , yielding a 4 wt % solution. The blends were subsequently recovered by precipitating them in 20-fold excess volume of methanol. The blends were washed with a large amount of methanol followed by drying in vacuo at  $100\text{ }^\circ\text{C}$  for 5 days.

Samples for the SAXS study were prepared by compression molding. The blend was compression molded by a hot press at  $280\text{ }^\circ\text{C}$  for 5 min followed by quenching into ice water to obtain an amorphous specimen of  $\sim 1$  mm thick. Subsequent crystallization was conducted at 210 and  $235\text{ }^\circ\text{C}$  on a Linkam HFS91 hot stage for 14 h.

**Differential Scanning Calorimetry.** Bulk crystallinities ( $\phi_c$ ) of PET/PEI blends were measured by a TA Instrument 2000 differential scanning calorimeter (DSC). The samples used for DSC measurement were cut directly from the sample disks for SAXS measurement. Crystallinity was calculated from the enthalpy of melting by taking the bulk enthalpy of melting of PET,  $\Delta H^0 = 138\text{ J/g}$ . The degree of crystallinity measured by DSC corresponds to the weight fraction of crystals ( $w_c$ ). Weight fraction was converted to volume fraction ( $\phi_c$ ) using a formula devised by Runt et al.<sup>7</sup>

**SAXS Measurement.** All SAXS measurements were performed at room temperature. The X-ray source, an 18 KW rotating anode X-ray generator (Rigaku) equipped with a rotating anode Cu target, was operated at 200 mA and 40 KV. The incident X-ray beam was monochromated by pyrolytic graphite, and a set of three pinhole inherent collimators were used so that the smearing effects inherent in slit-collimated small-angle X-ray cameras could be avoided. The sizes of the first and second pinhole were 1.5 mm and 1.0 mm, respectively, and the size of the guard pinhole before the sample was 2.0 mm. The scattered intensity was detected by a two-dimen-

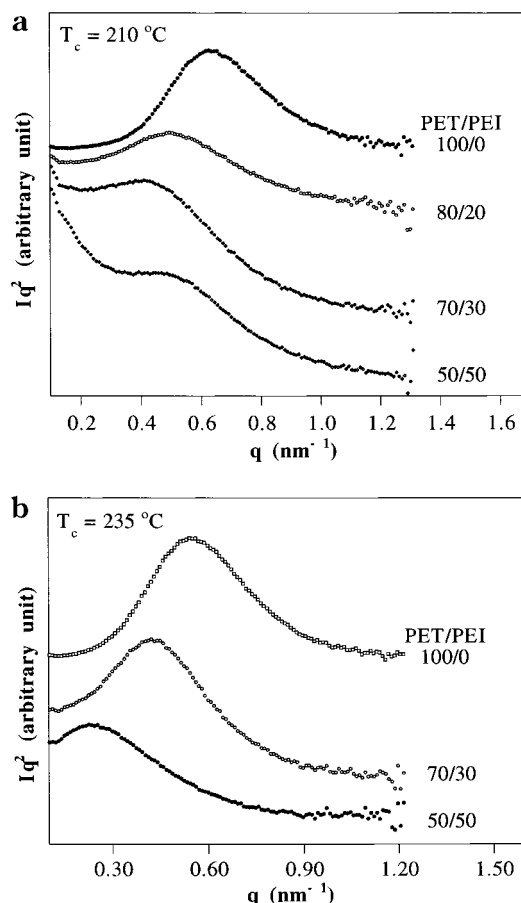


**Figure 1.** Lorentz-corrected intensity profiles of PET/PEI blends subjected to crystallization at (a)  $210\text{ }^\circ\text{C}$  and (b)  $235\text{ }^\circ\text{C}$  for 14 h. The blend compositions are indicated in the figure.

sional position sensitive detector (ORDELA Model 2201X, Oak Ridge Detector Laboratory Inc., Oak Ridge, CA) with  $256 \times 256$  channels (active area  $20 \times 20\text{ cm}^2$  with  $\sim 1$  mm resolution). The sample to detector distance was 4000 mm. The beam stop was around a lead disk of 18 mm diameter. All data were corrected by the background (dark current and empty beam scattering) and the sensitivity of each pixel of the area detector. The area scattering pattern was radially averaged to increase the efficiency of data collection compared with a one-dimensional linear detector. Data were acquired and processed on an IBM-compatible personal computer.

The intensity profile was further corrected by subtracting the background intensity associated with thermal density fluctuation by the application of the Porod–Ruland model<sup>22–25</sup>

$$I(q) = K_p \frac{\exp(-\sigma^2 q^2)}{q^4} + I_h \quad (1)$$

where  $I(q)$  is the recorded scattering intensity,  $q = 4\pi/\lambda \sin(\theta/2)$  ( $\theta$  = scattering angle),  $K_p$  is the Porod constant,  $\sigma$  is a parameter related to the thickness of crystal/amorphous interphase, and  $I_h$  is the background intensity arising from thermal density fluctuation. The values of  $K_p$ ,  $\sigma$ , and  $I_h$  were obtained by curve fitting the intensity profile at high  $q$  region ( $1.1\text{--}1.3\text{ nm}^{-1}$ ).

## Results and Discussion

Figure 1 shows the profiles of Lorentz-corrected intensity ( $I(q^2)$ ) of semicrystalline PET/PEI blends subjected to crystallization at 210 and  $235\text{ }^\circ\text{C}$  for 14 h. Pure PET exhibits a typical scattering peak associated with the electron density contrast between the alternating crystalline and amorphous layers. Semicrystalline PET/

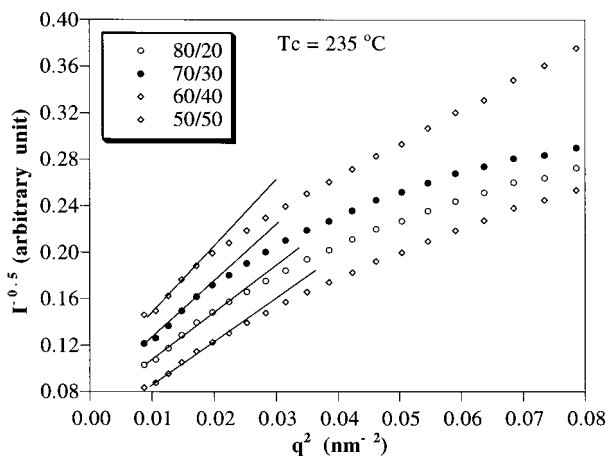


**Figure 2.** Debye–Bueche plots of PET/PEI blends crystallized at 235 °C. Good linearity is observed at low  $q$  region, whereas deviation from the initial linearity starts at  $q \approx 0.14 \text{ nm}^{-1}$ .

PEI blends display very different scattering patterns. For both crystallization temperatures ( $T_c$ ), the scattering intensity shows an abrupt increase at the low angular region. The intensity rise is more pronounced for blends with higher PEI composition. Instead of a monotonic decay with increasing  $q$ , the scattering patterns are characterized by the superposition of a monotonically decayed profile and a scattering peak associated with the alternating crystalline/amorphous layers. The large low  $q$  intensity signifies the presence of a heterogeneity with a larger size than the crystalline and amorphous layers. In parallel with the previous discussion for the PCL/PSO system, the low  $q$  intensity was attributed to the electron density contrast between the “lamellar stack domains (LS domains)” consisting of alternating crystalline/amorphous layers and the amorphous domains located outside the LS domains.<sup>16</sup> The exterior amorphous domains were likely induced by liquid–liquid demixing.

Provided that the LS domains and the exterior amorphous domains were randomly distributed and the scattering from the alternating layers within the LS domains is negligible at small  $q$ , the low- $q$  intensity should be closely described by the Debye–Bueche equation<sup>26</sup>

$$I(q) = \frac{A}{(1 + a_c^2 q^2)^2} \quad (2)$$

where  $A$  is a constant and  $a_c$  is the correlation length that is a measure of the scale of heterogeneity. Equation 2 prescribes that a plot of  $I^{-1/2}$  versus  $q^2$  should yield a straight line with the slope of  $a_c^2 A^{-1/2}$  and the intercept of  $1/A^{-1/2}$ . The correlation length can hence be calculated from the ratio of the slope to the intercept. Figure 2 shows the Debye–Bueche plots of semicrystalline PET/PEI blends. Good linearity is observed at the low  $q$  region, whereas deviation from the initial linearity starts at  $q \approx 0.14 \text{ nm}^{-1}$ . Good linearity in the plot signifies the applicability of the random two-phase description at the low  $q$  region; deviation at higher  $q$  is due to the contribution of the scattering associated with the alternating crystalline/amorphous layers. Table 1 lists the values of correlation lengths determined from the Debye–Bueche plots. The correlation length was  $\sim 8.1 \text{ nm}$ . It will be shown later that this value is larger than the thickness of the crystalline and amorphous

**Table 1.** Correlation Lengths ( $a_c$ ) Obtained from Debye–Bueche Plot for PET/PEI Blends Crystallized at 210 and 235 °C

PET/PEI composition	$a_c$ (nm)	
	$T_c = 210 \text{ °C}$	$T_c = 235 \text{ °C}$
80/20	8.2	8.0
70/30	8.4	7.0
60/40	7.7	8.7
50/50	9.3	7.7

layers, which suggests the blends had developed a heterogeneity with larger size than the two types of layers.

To provide further details on the morphological structure, the morphological parameters associated with the LS domains, including the crystal thickness ( $l_c$ ), amorphous layer thickness ( $l_a$ ), and long period ( $L = l_c + l_a$ ) must be evaluated. Two approaches are typically adopted for this purpose. One is to fit the SAXS profile using the established models such as the Hosemann–Tsvankin model<sup>27</sup> and the Vonk–Kortleve model<sup>28,29</sup> for lamellar stacks; the morphological parameters can be obtained from the curve fit. The other approach is to perform the Fourier transform for the SAXS profile to yield the one-dimensional correlation function [ $\gamma(z)$ ] or the interphase distribution function [IDF,  $g_1(z)$ ] in real space. The one-dimensional correlation function is defined as<sup>30</sup>

$$\gamma(z) = \frac{1}{\gamma(0)} \int_0^\infty I(q) q^2 \cos(qz) dq \quad (3)$$

where  $\gamma(0)$  is just the scattering invariant

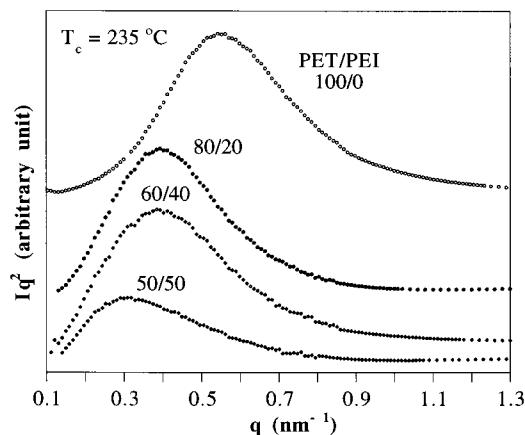
$$Q = \int_0^\infty I q^2 dq \quad (4)$$

The interphase distribution function is given by the second derivative of  $\gamma(z)$ ; viz.  $g_1(z) = \gamma''(z)$ .<sup>8,19–21</sup> The morphological parameters may be deduced from the maxima and minima and through simple geometric analysis of  $\gamma(z)$  and  $g_1(z)$ .<sup>8,19–21,30</sup>

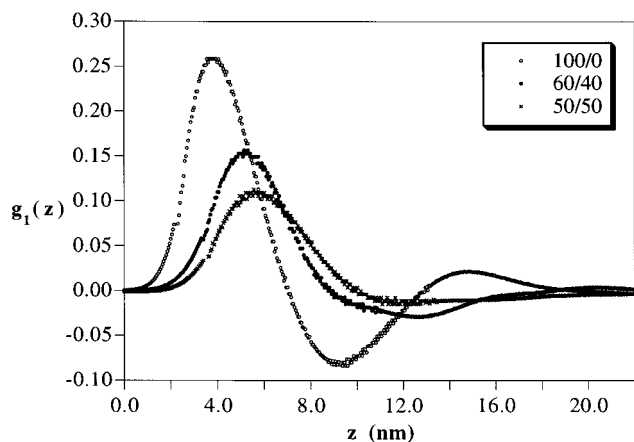
Because of the complication by the additional scattering at low  $q$  region, the two approaches just outlined cannot be applied directly to PET/PEI blends. For the PCL/PSO system, Nojima et al.<sup>15–17</sup> used a combination of Hosemann–Tsvankin model and Debye–Bueche equation to fit the experimental SAXS profiles, where the morphological parameters were obtained from the curve fit. An alternative approach is utilized in this study. In the present method, the entire scattering profile arising from the electron density contrast between the LS domains and the exterior amorphous domains was first calculated by Debye–Bueche equation. This intensity contribution was subtracted from the overall scattering profile to yield the scattering pattern stemming solely from the alternating crystalline/amorphous layers. The resultant pattern was subsequently Fourier transformed to the one-dimensional correlation function. Because the positions of minimum and maximum in the correlation function may be perturbed by the broad size distribution of the lamellae, the one-dimensional correlation function was further converted into the interphase distribution function, through which the morphological parameters can be more reliably determined.<sup>19</sup>

Figure 3 compares the scattering patterns of PET/PEI blends after eliminating the Debye–Bueche con-





**Figure 3.** Lorentz-corrected intensity profiles of PET/PEI blends after eliminating the Debye–Bueche contribution. The SAXS profiles are characterized by a peak that is associated with the scattering from the alternating crystalline/amorphous layers.



**Figure 4.** Interphase distribution functions of PET/PEI blends crystallized at 235 °C. The first minimum provides the value of long period and the first maximum yields the thickness of either crystalline or amorphous layer.

tribution. Under these conditions, the SAXS profiles are characterized by a peak. The peak position ( $q_{\max}$ ) shifts to lower angle upon blending with PEI, implying that the long period computed from the Bragg's law increases upon blending. Figure 4 presents the interphase distribution functions for the blends crystallized at 235 °C. The first minimum of IDF provides the value of the long period, and the first maximum yields the thickness of either the crystalline or amorphous layer. Based on Babinet's reciprocity theorem,<sup>31</sup> it is not possible to distinguish whether the first maximum corresponds to  $l_c$  or  $l_a$ . Therefore, the smaller length deduced from the first maximum is denoted by  $l_1$  and the larger length given by  $L - l_1$  is denoted by  $l_2$ . Figure 5 displays the composition variations of  $l_1$  and  $l_2$  for the two crystallization temperatures. For  $T_c = 210$  °C,  $l_1$  remains approximately constant, whereas  $l_2$  increases with PEI composition and then levels off at  $\sim 7.0$  nm. Both  $l_1$  and  $l_2$  increase upon blending, but the tendency also levels off for the blends crystallized at 235 °C.

The assignment of  $l_1$  and  $l_2$  is governed by the linear crystallinity,  $\phi_c^{\text{lin}}$ , which is defined as

$$\phi_c^{\text{lin}} = \frac{l_c}{L} = \frac{l_c}{l_c + l_a} \quad (5)$$

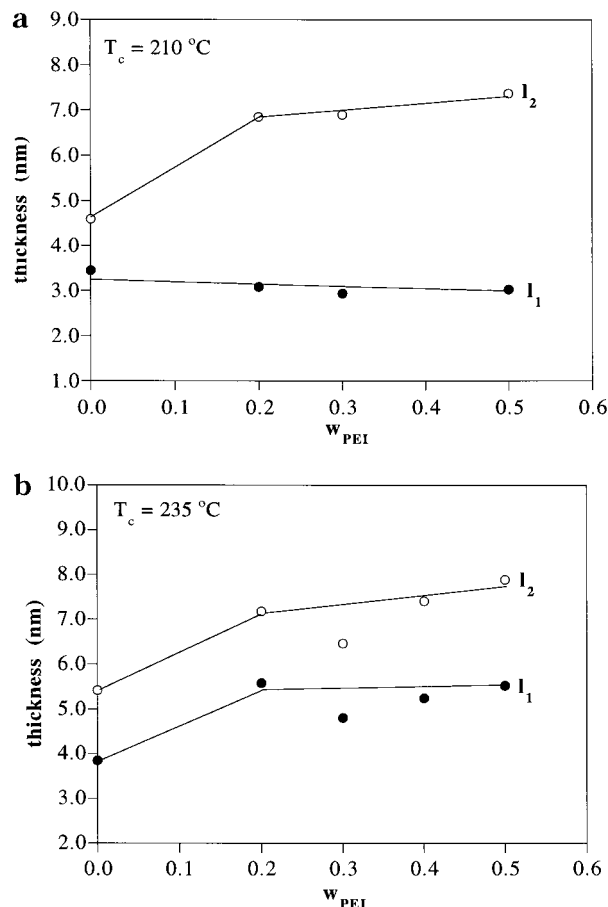


**Figure 5.** Composition variations of the smaller length ( $l_1$ ) and the larger length ( $l_2$ ) deduced from the interphase distribution function for PET/PEI blends crystallized at (a) 210 °C and (b) 235 °C.

When the linear crystallinity is  $<0.5$ , the crystals contribute to the smaller thickness, thus,  $l_1 = l_c$  and  $l_2 = l_a$ . The inverse is true for  $\phi_c^{\text{lin}} > 0.5$ . The linear crystallinity is related to the bulk crystallinity,  $\phi_c$  (i.e., the crystallinity measured by density or thermal analysis) by

$$\phi_c = \phi_s \phi_c^{\text{lin}} \quad (6)$$

where  $\phi_s = \phi_c / \phi_c^{\text{lin}}$ , the volume fraction of lamellar stacks in the sample. Equation 6 is valid only when the spherulites are volume filling. Because  $\phi_s \leq 1$ , eq 6 prescribes that the bulk crystallinity cannot be higher than the linear crystallinity. Consequently, the assignment of  $l_1$  and  $l_2$  would be rather straightforward if the bulk crystallinity is  $>0.5$  because, in this case, the larger length,  $l_2$ , must correspond to the crystal thickness and  $l_1$  must correspond to the amorphous layer thickness. Unfortunately, the bulk crystallinities of all PET and PET/PEI blends were  $<0.5$ , where the  $\phi_c$  of pure PET was 0.45 and 0.44 for  $T_c = 210$  and 235 °C, respectively, and  $\phi_c$  of the blends was even lower.

The assignments of  $l_1$  and  $l_2$  for PET/PEI blends may actually be facilitated by the following conditions:

(1) A previous study has pointed out that the equilibrium melting point depression of PET/PEI blends was very small.<sup>32</sup> Given that the observed melting points are independent of blend composition for samples crystallized at both temperatures, the crystal thickness is expected to remain constant.

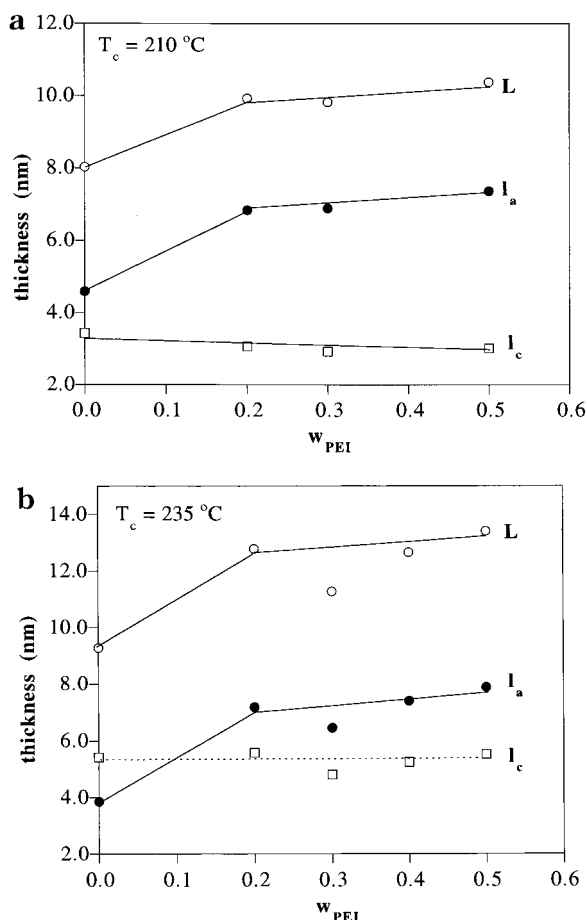


**Figure 6.** Composition dependences of crystal thickness ( $l_c$ ), amorphous layer thickness ( $l_a$ ), and long period ( $L$ ) of PET/PEI blends crystallized at (a) 210 °C and (b) 235 °C.

(2) The crystal thickness formed at 235 °C must be larger than that formed at 210 °C.

Based on these two conditions, we assigned  $l_1$  as the crystal thickness and  $l_2$  as the amorphous layer thickness for all compositions crystallized at 210 °C, because it was found in Figure 5(a) that  $l_1$  remained constant with composition. As to  $T_c = 235\text{ °C}$ , if the same assignments for  $T_c = 210\text{ °C}$  were applied to all compositions, the crystal thickness would have increased upon blending [Figure 5(b)] which clearly violates the first condition. Consequently, the assignment for pure PET was exchanged so that  $l_1$  corresponds to  $l_a$  and  $l_2$  to  $l_c$ . Such an exchanged assignment leads to a constant  $l_c$  for  $T_c = 235\text{ °C}$ . Figure 6 plots the assigned crystal thickness, amorphous layer thickness, and the long period against PEI composition. The crystal thickness is larger at 235 °C, which supports that the assignments of  $l_1$  and  $l_2$  are appropriate.

Figure 6 demonstrates that the blends have a larger amorphous layer thickness than pure PET, meaning that PEI was expelled to the interlamellar regions after crystallization. Despite the swelling of amorphous layers, the thickness is relatively independent of the overall blend composition, where all blends exhibit approximately the same  $l_a$ . A similar phenomenon has also been observed in PCL/PSO system.<sup>15,16</sup> Because a complete interlamellar incorporation should result in a monotonic increase of amorphous layer thickness with PEI composition, the observation implies an incomplete incorporation of PEI into the interlamellar regions. In other words, some PEI molecules were expelled out of

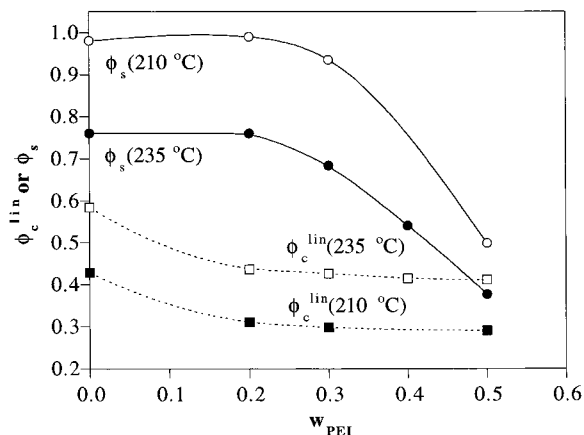


**Figure 7.** Dependences of linear crystallinity ( $\phi_c^{\text{lin}}$ ) and volume fraction of lamellar stacks ( $\phi_s$ ) of PET/PEI blends crystallized at the temperatures indicated in the figure.

the interlamellar regions and consequently resided outside the LS domains (the extralamellar placement). The extralamellar placement of PEI created the exterior amorphous domains, giving rise to the high scattering intensity at low  $q$ .

The extent of interlamellar incorporation of PEI can be further evaluated from the volume fraction of lamellar stacks,  $\phi_s$ .<sup>8</sup> In the case of complete interlamellar incorporation, the whole sample is homogeneously filled with lamellar stacks and, hence,  $\phi_s = 1$ . A larger extent of extralamellar placement will result in smaller  $\phi_s$ . The variation of  $\phi_s$  with PEI composition is displayed in Figure 7, where  $\phi_s$  was computed from the ratio of bulk crystallinity to linear crystallinity. The value of  $\phi_s$  of pure PET crystallized at 210 °C is around unity. Crystallization of pure PET at this temperature thus yielded homogeneously filled lamellar stacks. On the other hand,  $\phi_s$  falls to 0.76 at  $T_c = 235\text{ °C}$ , implying that even pure PET was not homogeneously filled with lamellar stacks at this temperature. For both crystallization temperatures,  $\phi_s$  remains approximately constant when the composition of PEI was <20 wt %. In this case, PEI molecules were predominantly incorporated into the interlamellar zones. The value of  $\phi_s$  drops when PEI composition exceeds 20 wt %, indicating the occurrence of significant extralamellar placement above this composition.

The morphological structure of semicrystalline PET/PEI blends has thus been established from Figures 6 and 7. As the composition of PEI fell below 20 wt %, PEI molecules were predominantly expelled into the interlamellar zones upon the crystallization of PET. Significant segregation of PEI out of the interlamellar regions occurred as the composition exceeded 20 wt %. Because approximately the same amorphous layer thickness was observed for all blends investigated, the composition of the interlamellar amorphous layer is regarded as independent of the overall composition.

Segregation of amorphous diluent during crystallization is natural because the driving force of crystallization tends to separate the two components from being mixed. It has been suggested that the diluent molecules confined in the interlamellar regions are deformed by the crystals and have lower conformational entropy. An entropic driving force is thus developed, which tends to pull the diluent molecules out of the interlamellar regions.<sup>7,33</sup> Judging from the observation that the compositions in the interlamellar regions are about the

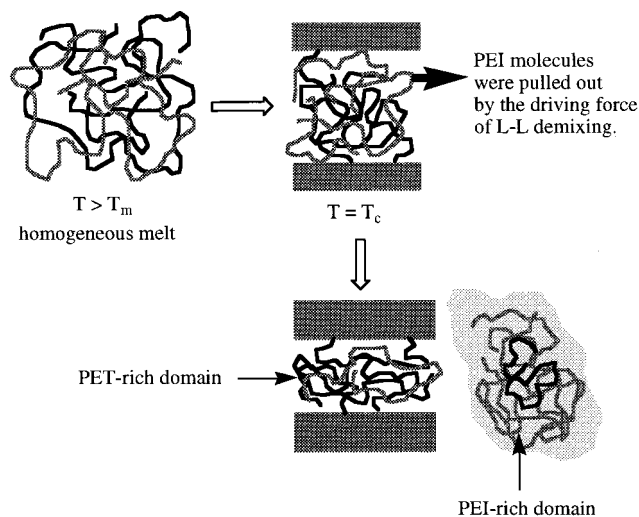


**Figure 8.** Schematic illustration of the morphological formation in PET/PEI blends. During the crystallization, the liquid–liquid demixing exerted a driving force to pull a portion of PEI out of the interlamellar regions to form PEI-rich domains outside the LS domains. The interlamellar regions thus represent the PET-rich phase and have approximately the same thickness irrespective of the overall composition.

same for all blends investigated, it is suggested that the driving force of liquid–liquid demixing dominated the segregation behavior of PEI. The formation of morphological structure in PET/PEI blends is proposed in Figure 8. As crystallization was taking place simultaneously with liquid–liquid demixing, the driving force of liquid–liquid demixing would inhibit the formation of a homogeneous mixture inside the interlamellar regions as long as the interlamellar amorphous phase is located in the unstable regions of the phase diagram ( $0.2 \leq w_{\text{PEI}} \leq 0.8$ , as estimated in the previous study). Consequently, liquid–liquid demixing may exert another driving force to pull a portion of PEI out of the interlamellar regions to form PEI-rich domains outside the LS domains, leaving the interlamellar zones as the PET-rich phase. Because of the binodal line prescribed by the phase diagram, the thickness and composition of the interlamellar PET-rich phase are independent of the overall blend composition.

## Conclusions

The morphological structure of semicrystalline PET/PEI blends has been investigated by SAXS. The occurrence of liquid–liquid demixing generated the PEI-rich domains that were located exterior to the LS domains. The electron density contrast between LS domains and the PEI-rich domain resulted in a strong scattering intensity at the low angular region. The crystal thickness of PET was relatively unperturbed by blending with PEI. When the composition of PEI was <20 wt %, PEI molecules were predominantly incorporated into the interlamellar regions upon the crystallization of

PET. When the PEI composition exceeded 20 wt %, significant extralamellar placement of PEI occurred and led to approximately constant amorphous layer thickness. It is suggested that the liquid–liquid demixing exerted a driving force to pull a portion of PEI out of the interlamellar regions to form the exterior PEI-rich domains. The interlamellar regions thus represent the PET-rich phase and have approximately the same thickness irrespective of the overall blend composition.

**Acknowledgment.** The support of this work by the National Science Council of the Republic of China under grant NSC 87-2216-E-007-046 is gratefully acknowledged.

## References and Notes

- (1) Khambata, F. B.; Warner, F.; Russell, T.; Stein, R. S. *J. Polym. Sci., Polym. Phys. Ed.* **1976**, *14*, 1391.
- (2) Warner, F. P.; MacKnight, W. J.; Stein, R. S. *J. Polym. Sci., Polym. Phys. Ed.* **1977**, *15*, 2113.
- (3) Ong, C. J.; Price, F. P. *J. Polym. Sci., Polym. Symp. Ed.* **1978**, *63*, 59.
- (4) Sadocco, P.; Canetti, M.; Seves, A.; Martuscelli, E. *Polymer* **1993**, *34*, 3368.
- (5) Cheung, Y. W.; Stein, R. S. *Macromolecules* **1994**, *27*, 2512.
- (6) Cheung, Y. W.; Stein, R. S.; Lin, J. S.; Wignall, G. D. *Macromolecules* **1994**, *27*, 2520.
- (7) Talibuddin, S.; Wu, L.; Runt, J. *Macromolecules* **1996**, *29*, 7529.
- (8) Chen, H.-L.; Li, L.-J.; Lin, T.-L. *Macromolecules* **1998**, *31*, 2255.
- (9) Tanaka, H.; Nishi, T. *Phys. Rev. Lett.* **1985**, *55*, 1102.
- (10) Inaba, N.; Sato, K.; Suzuki, S.; Hashimoto, T. *Macromolecules* **1986**, *19*, 1690.
- (11) Inaba, N.; Yamada, T.; Suzuki, S.; Hashimoto, T. *Macromolecules* **1988**, *21*, 407.
- (12) Tanaka, H.; Nishi, T. *Phys. Rev. A* **1989**, *39*, 783.
- (13) Burghardt, W. R. *Macromolecules* **1989**, *22*, 2482.
- (14) Li, Y.; Jungnickel, B.-J. *Polymer* **1993**, *34*, 9.
- (15) Nojima, S.; Terashima, Y.; Ashida, T. *Polymer* **1986**, *27*, 1007.
- (16) Nojima, S.; Satoh, K.; Ashida, T. *Macromolecules* **1991**, *24*, 942.
- (17) Nojima, S.; Kato, K.; Ono, M.; Ashida, T. *Macromolecules* **1992**, *25*, 1922.
- (18) Chen, H.-L. *Macromolecules* **1995**, *28*, 2845.
- (19) Santa Cruz, C.; Stribeck, N.; Zachmann, H. G.; Balta' Calleja, F. J. *Macromolecules* **1991**, *24*, 5980.
- (20) Albrecht, T.; Strobl, G. *Macromolecules* **1995**, *28*, 5827.
- (21) Albrecht, T.; Strobl, G. *Macromolecules* **1996**, *29*, 783.
- (22) Ruland, W. J. *J. Appl. Crystallogr.* **1971**, *4*, 70.
- (23) Porod, G. *Koll. Z.* **1951**, *124*, 83.
- (24) Porod, G. *Koll. Z.* **1952**, *125*, 51.
- (25) Porod, G. *Koll. Z.* **1952**, *125*, 108.
- (26) Debye, P.; Bueche, A. M. *J. Appl. Phys.* **1949**, *20*, 518.
- (27) Hosemann, R.; Bagchi, S. N. *Direct Analysis of Diffraction by Matter*; North-Holland: Amsterdam, 1962.
- (28) Vonk, C. G. in *Small-Angle X-ray Scattering*; Glatter, O.; Kratky, O., Eds; Academic: New York, 1982.
- (29) Vonk, C. G.; Kortleve, G. *Kolloid Z. Z. Polym.* **1967**, *220*, 19.
- (30) Strobl, G. R.; Schneider, M. *J. Polym. Sci., Polym. Phys. Ed.* **1980**, *18*, 1343.
- (31) Cowley, J. M. *Diffraction Physics*, 2nd ed.; North-Holland: Amsterdam, 1981.
- (32) Chen, H.-L.; Hwang, J. C.; Chen, C.-C. *Polymer* **1996**, *37*, 5461.
- (33) Russell, T. P.; Ito, H.; Wignall, G. D. *Macromolecules* **1988**, *21*, 1703.

MA980700C